

Vicarious Cold Calibration for Conical Scanning Microwave Imagers

Rachael A. Kroodsma, *Member, IEEE*, Darren S. McKague, and Christopher S. Ruf, *Fellow, IEEE*

Abstract—Vicarious cold calibration (VCC) for spaceborne microwave radiometers is analyzed and modified for application to conical scanning microwave imagers at frequencies from 6 to 90 GHz. The details of the algorithm are modified to account for additional frequencies and polarizations that were not included in the development of the original algorithm. The modified algorithm is shown to produce a more stable cold reference brightness temperature (TB) than the original algorithm. An analysis is performed of this updated algorithm to show the global regions that contribute to the derivation of the cold reference TB and to show which geophysical parameters contribute to the coldest TBs. The analysis suggests that water vapor variability has the largest impact on the TBs in the VCC algorithm. The modified VCC algorithm is applied to microwave imager data and is used as an intercalibration method. It is shown to agree well with other intercalibration methods, demonstrating that it is a valid and accurate method for calibration of microwave imagers.

Index Terms—AMSR2, calibration, intercalibration, Microwave radiometry, TMI.

I. INTRODUCTION

MICROWAVE radiometers onboard satellites provide valuable observations of the earth's surface and atmosphere. These observations are in the form of brightness temperature (TB) measurements that are input to models to retrieve numerous geophysical parameters, such as surface temperature, surface wind speed (SWS), and atmospheric water vapor. In order to retrieve accurate geophysical parameters, the radiometer TB measurements must first be properly calibrated before they are used as inputs to geophysical retrieval algorithms. Microwave radiometers typically have an on-board calibration system to calibrate the instrument while it is in flight to convert from raw counts into antenna temperatures. The antenna temperatures are then converted into TBs through an antenna pattern correction. In addition to the on-board calibration of the radiometer, the TBs measured from the earth can also be used to monitor the calibration of the radiometer. Using these TBs provides a calibration reference

Manuscript received January 20, 2016; revised June 24, 2016; accepted August 24, 2016. Date of publication October 24, 2016; date of current version December 29, 2016.

R. A. Kroodsma is with the Earth System Science Interdisciplinary Center, University of Maryland, College Park, MD 20740 USA, and also with the NASA Goddard Space Flight Center, Greenbelt, MD 20771 USA (e-mail: rachael.a.kroodsma@nasa.gov).

D. S. McKague and C. S. Ruf are with the University of Michigan, Ann Arbor, MI 48109 USA (e-mail: dmckague@umich.edu; cruf@umich.edu).

Color versions of one or more of the figures in this paper are available online at <http://ieeexplore.ieee.org>.

Digital Object Identifier 10.1109/TGRS.2016.2615552

for the instrument that is performed through the radiometer's reflector and can be used to detect calibration issues such as errors in the antenna pattern correction, obstructions in the field of view, or drifts in the on-board calibration system.

Vicarious cold calibration (VCC) is one method that uses an external earth target to calibrate a spaceborne microwave radiometer [1]. VCC uses histograms of the TB observations to derive a stable cold reference point, referred to as the "cold cal TB." VCC has been shown to be a valuable tool for microwave radiometer calibration by detecting drifts in the radiometer measurements [2], correcting obstructions in the field of view [3], and deriving intercalibration offsets [4], [5]. Previous studies [3]–[5] applied VCC to conical scanning microwave imagers, even though the original algorithm described in [1] was for use with a nadir-viewing microwave radiometer over a more narrow range of frequencies. These studies used a modified VCC algorithm different from the original and obtained quality results, but the changes made to the algorithm were not described nor was the modified algorithm analyzed to confirm that it was better able to achieve a stable cold cal TB in the conical scanning case.

This paper discusses the application of VCC to conical scanning microwave imagers and provides an in-depth analysis of various aspects of the VCC algorithm, including a description of how the VCC algorithm is modified. First, the VCC algorithm details are examined and modifications are made to the original algorithm to make it applicable to conical scanners. Second, the geophysical parameters that contribute to the derivation of the cold cal TB are examined. Third, the VCC algorithm is applied to microwave imager data to show its use as a relative calibration tool. Finally, the modified VCC algorithm is validated by using it to intercalibrate microwave radiometers and demonstrate that it achieves comparable results with other intercalibration methods.

II. VCC ALGORITHM

The original VCC algorithm was designed to be used with a nadir-viewing microwave radiometer at 18, 21, and 37 GHz [1]. The algorithm derives a stable cold reference using TB histograms of over-ocean observations. To derive this cold reference, a "first-guess" value is found for each frequency. This is the theoretical coldest TB derived from a radiative transfer model (RTM). The radiometer observed TBs that fall within ± 10 K of this first-guess are binned into histograms for each channel at 0.1 K intervals. A third-degree polynomial is then fit to 3%–10% of the cumulative distribution function (CDF) of this histogram and the polynomial is

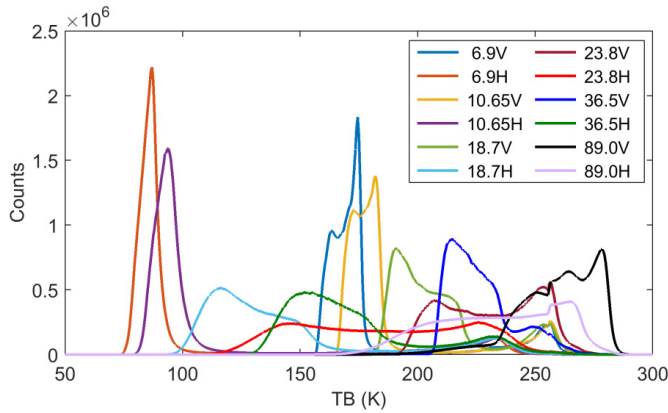


Fig. 1. AMSR2 TB histograms for one month of over-ocean observations.

extrapolated down to 0%, where the TB value at 0% CDF is the cold cal TB. These details of the original VCC algorithm were chosen to achieve the most stable cold reference for a specific nadir-viewing radiometer. However, these details may not result in the most stable cold cal TB for conical scanning imagers. This section discusses modifications that are made to the original VCC algorithm to make it applicable to conical scanning imagers and shows the improvement of the modified algorithm over the original one.

A. Conical Scanning Microwave Imager Observations

One major difference between conical scanning and nadir-viewing radiometers is the angle at which they view the earth. Conical scanners have a reflector that is offset from nadir, resulting in a nonzero earth incidence angle (EIA) and a signal received from earth's surface that is polarized. A second major difference is the polarization of the TB measurements. Conical scanners observe distinct vertical (V) and/or horizontal (H) polarized TBs at each frequency while nadir-viewing radiometers do not observe a polarized signal. The frequencies of conical scanners vary for each instrument based on specific design requirements but most have frequencies near 18, 21, and 37 GHz. Other frequencies typically included are near 7, 11, and 90 GHz, so all of these frequencies should be considered when developing a new VCC algorithm. Conical scanners can include frequencies higher than 90 GHz; however, these frequencies see less of the surface due to a higher sensitivity to the atmospheric water vapor. This makes it very difficult for VCC to derive a stable cold reference, so these higher frequencies are not discussed here.

The VCC algorithm calculates the cold cal TB from histograms of over-ocean TBs. The shape of the histograms can influence the stability of the cold cal TB, so it is valuable to examine how the histograms differ as a function of frequency and polarization. This is shown here using TB observations from the Advanced Microwave Scanning Radiometer 2 (AMSR2). AMSR2 is a conically scanning microwave radiometer that observes at 6.925, 7.3, 10.65, 18.7, 23.8, 36.5, and 89.0 GHz, with vertical and horizontal polarizations at all frequencies [6]. Fig. 1 shows TB histograms for one month of over-ocean observations for 12 of the 16 AMSR2 channels.

The 7.3 and 89.0b GHz channels are excluded since they are nearly identical to the 6.925 and 89.0a GHz channels, respectively.

Fig. 1 illustrates the variation in the TB histograms across the frequency spectrum. Some of the channels, such as 6.9 and 10.65 H, show one very steep peak with the majority of the observations occurring over a small range of TBs, while other channels, such as 23.8 and 89.0 H, have histograms with a more uniform distribution across a wide dynamic range of TBs. Since the shapes of the histograms vary by channel, the best VCC algorithm will most likely be different, depending on the channel to which the algorithm is applied.

B. Development of Modified VCC Algorithm

This section describes the development of the modified VCC algorithm for application to conical scanners. The application of the modified algorithm to AMSR2 is shown as an example.

1) *Algorithm Details:* The VCC algorithm can be divided into four steps: 1) calculate a first-guess for each channel; 2) bin the TBs into histograms for a range of ± 10 K from the first-guess; 3) calculate the CDF for each histogram and take 3%–10% of the CDF (called the CDF subset); and 4) fit a third-order polynomial to the inverse CDF subset and extrapolate down to 0%. Each of these steps encompasses a detail of the VCC algorithm that is analyzed for modification. The details for each step are identified as: 1) how the first-guess is calculated; 2) the choice of the ± 10 K TB range; 3) the choice of 3%–10% for a CDF subset; and 4) the choice of a third-order polynomial fit.

The first step in deriving the cold cal TB using the original VCC algorithm is to calculate a first-guess value for all the channels. The radiometer TBs are then binned into histograms based off this first-guess. It is ideal to eliminate this step and instead have the algorithm depend solely on the TB histograms. There are three reasons for this as follows.

- 1) For each radiometer that is calibrated using VCC, a new first-guess has to be calculated (based on individual frequency, polarization, and EIA of the instrument).
- 2) This first-guess is not stable with respect to time.
- 3) The theoretical minimum TB that is used as the first-guess usually does not exist on earth, especially for frequencies most sensitive to atmospheric water vapor and SWS.

This causes the theoretical minimum TB in some cases to be several Kelvin below the observed minimum TB of the radiometer, creating instability in the VCC algorithm. A more ideal approach is to find a first-guess based on the histogram or eliminate the need for a first-guess altogether.

The first-guess that is calculated using an RTM assuming ideal cold conditions (calm ocean and dry atmosphere) may not actually exist. If a first-guess is chosen that is too low, the desired TBs will not get binned into the histograms. Table I gives an example of how small changes in the geophysical parameters can impact the first-guess. The first-guess is calculated as the minimum TB that occurs over-ocean using a standard atmosphere for three different cases. Case 1 uses the following conditions at the surface: 288 K temperature,

TABLE I

MINIMUM TB MODELED USING AN RTM WITH STANDARD ATMOSPHERE AND VARYING IWV AND SWS. THE MAXIMUM DIFFERENCE AMONG THE THREE CASES IS SHOWN IN THE LAST COLUMN

Channel	Case 1 (K) 0 cm IWV 0 m/s SWS	Case 2 (K) 0.5 cm IWV 0 m/s SWS	Case 3 (K) 0 cm IWV 5 m/s SWS	Max Diff (K)
6.9V	146.8	146.9	146.6	0.3
6.9H	72.4	72.6	75.5	3.1
10.65V	156.1	156.4	155.8	0.6
10.65H	77.6	78.1	81.2	3.6
18.7V	170.6	173.3	170.3	3.0
18.7H	86.8	91.7	91.4	4.9
23.8V	178.2	186.4	177.9	8.5
23.8H	92.7	107.8	97.6	15.1
36.5V	197.8	199.9	197.3	2.6
36.5H	113.6	117.8	119.6	6.0
89.0V	229.9	234.1	228.4	5.7
89.0H	135.5	151.5	143.1	16.0

1013 mb pressure, and 0 m/s ocean SWS with 0 cm integrated water vapor (IWV). Case 2 increases the IWV to 0.5 cm, leaving the other conditions the same. Case 3 uses the same conditions as Case 1 except increasing the SWS to 5 m/s. The sea surface temperature (SST) is varied and the minimum TB at each frequency is shown in Table I for the three cases along with the maximum difference among the cases. The RTM uses the Meissner and Wentz [7] ocean surface emissivity model along with Rosenkranz's [8] water vapor and Liebe *et al.*'s [9] oxygen absorption models.

Table I reveals that small deviations from a calm ocean or in the water vapor burden will cause significant changes in TB for those channels most sensitive to SWS and IWV. The channels most sensitive to water vapor, 23.8 and 89.0 H, increase by approximately 15 K with the addition of 0.5 cm IWV. Small changes in the geophysical conditions result in large changes in TB for these channels. This is one of the reasons that the original VCC algorithm may not work properly if the first-guess is found using an RTM. This example shows that changing the geophysical conditions only slightly causes the minimum TB to be outside the ± 10 K range of the histogram used for deriving the cold cal TB.

Another detail of the VCC algorithm to be examined is the range of TBs from the histogram used in Step 2. The original algorithm bins TBs into a histogram that fall within ± 10 K of the first-guess. Fig. 2 shows the cold ends of the histograms from Fig. 1 for three channels: 10.65, 18.7, and 23.8 H. The histograms are shown as a function of the TB difference from TB_{min} , where TB_{min} is defined as the TB at 0.5% of the CDF for each TB histogram. The TB_{min} values for 10.65, 18.7, and 23.8 H are 82.7, 100.2, and 119.5 K, respectively. Fig. 2 shows that the shape of the histogram can differ greatly from one channel to another, so the details in Step 2 of the VCC algorithm may need to be modified to account for this.

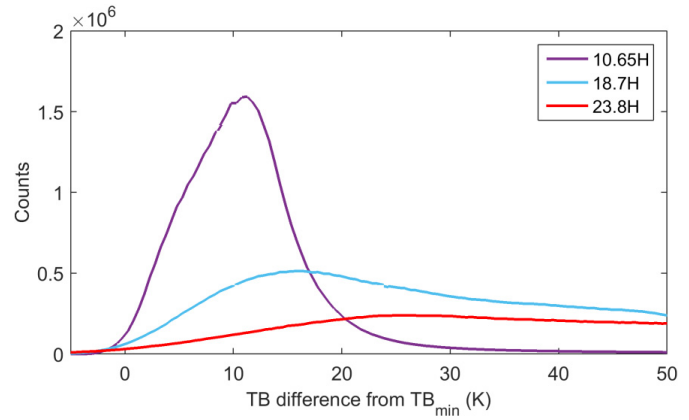


Fig. 2. AMSR2 TB histograms for 10.65, 18.7, and 23.8 H for July 2014 where TB_{min} for each channel is 82.7, 100.2, and 119.5 K, respectively.

The other details of the VCC algorithm in Steps 3 and 4 are the range chosen for the CDF subset and the degree of polynomial. These details will be examined later as they are dependent on the histogram range chosen for Step 2.

2) *Procedure*: A modified VCC algorithm is chosen based on its ability to calculate a stable cold cal TB. "Stable" implies a cold cal TB that is independent of geophysical effects such as atmospheric water vapor variations. Table I shows that small changes in the geophysical parameters can have a large impact on the TB. We want to minimize the impact of geophysical variation on the cold cal TB, thus creating a stable reference that can be used for calibration. As seen in Table I, certain channels (e.g., 23.8 H) are more sensitive than others to the geophysical variability, so these channels may not achieve as stable a reference as other channels (e.g., 6.9 V).

One way to test the stability of the VCC algorithm is to apply the algorithm to a situation with an expected result. The observed TBs are impacted not only by geophysical variation but also by instrument calibration and spacecraft characteristics (e.g., attitude offsets), which can all affect the cold cal TB. Testing of the VCC algorithm stability using observed TBs introduces the possibility that instrument calibration instability would confuse interpretation of the results. Therefore, modeled TBs from an RTM are used to simulate the radiometer observed TBs, so instrument calibration issues will not be a factor. A comparison of AMSR2 observed (obs) and simulated (sim) TB histograms is shown in Fig. 3 for three channels. The observed and simulated total TB histograms are different since the RTM does not model clouds or precipitation, and errors in the RTM or instrument calibration can cause the offset seen between the histograms. However, the cold ends of the histograms have a very similar shape, which implies that even though the VCC algorithm is derived using simulated TBs, it will behave similarly when applied to the observed TBs.

Conical scanning radiometers take measurements at a certain number of pixels across the part of the scan that views the earth. Assuming that the radiometer views the earth at a constant EIA across the scan, the cold cal TB calculated for each scan position should be equal, allowing that sufficient data are used in the calculation to negate the geophysical

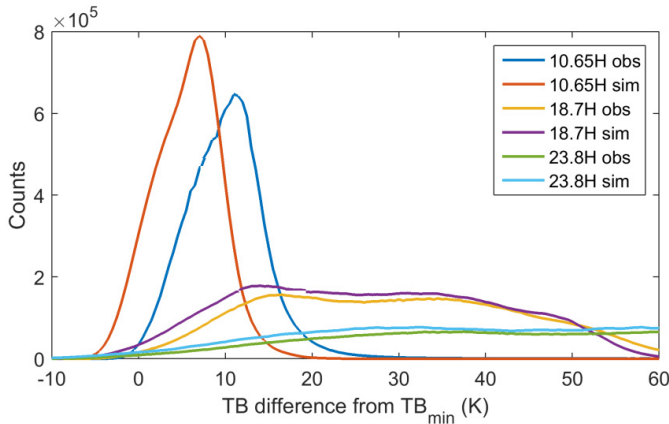


Fig. 3. AMSR2 observed and simulated TB histograms for 10.65, 18.7, and 23.8 H for July 2014 where TB_{\min} for each channel is 82.7, 100.2, and 119.5 K, respectively. The observed and simulated total TB histograms are different but the cold end shapes are similar.

variability. Deviations from the mean cold cal TB across the scan indicate instability in the VCC algorithm. Therefore, the standard deviation of the simulated cold cal TB across the scan can be used as a metric for determining the stability of the VCC algorithm. For this paper, AMSR2's frequencies, nominal EIA (55°), orbit, and scanning geometry are used since these features are typical of conical scanning radiometers.

C. Modified VCC Algorithm

TBs are simulated for one month (July 2014) of AMSR2 over-ocean observations using a constant EIA of 55° for all pixels. The RTM used to simulate the TBs is described in detail in [4]. Ancillary data are provided from the Global Data Assimilation System (GDAS) [10]. The TBs are binned into histograms for each channel and various tests are performed on the histograms to determine the best version of the VCC algorithm for each channel.

Table II gives a sample of the results showing how the modified VCC algorithm details were chosen. The standard deviation of the cold cal TB across the scan is given for various TB ranges (Step 2), CDF subset minimum values (Step 3), and polynomial order (Step 4) for 10.65, 18.7, and 23.8 H. These channels are chosen to represent the other AMSR2 channels since the 12 channels can be placed into three groups that all have similar histogram shapes at the cold end: 6.9 V/H, 10.65 V/H, 18.7 V, and 36.5 V in Group 1, 18.7 H, 23.8 V, 36.5 H, and 89.0 V in Group 2, and 23.8 and 89.0 H in Group 3. The first-guess (Step 1) is taken as 0.5% of the total TB histogram and the CDF subset maximum value (Step 3) is 10%. 0.5% is chosen for the first-guess since it is sufficiently small to capture the TB near the minimum of the histogram but not too small to be impacted by any noise in the TB histogram at the cold end. 10% is chosen for the CDF maximum value since this was used in the original algorithm and adjusting the maximum CDF values from 10% by a few percentages does not significantly change the results. The values in bold text in Table II indicate standard deviations that are within 0.05 K of the minimum value for each channel.

TABLE II
STANDARD DEVIATION OF COLD CAL TB ACROSS THE SCAN FOR VARIOUS ALGORITHM PARAMETERS FROM STEPS 2, 3, AND 4 FOR CHANNELS 10.65, 18.7, AND 23.8 H FOR JULY 2014 SIMULATED DATA. BOLD NUMBERS INDICATE STANDARD DEVIATIONS THAT ARE WITHIN 0.05 K OF THE MINIMUM VALUE AMONG THE VARIOUS PARAMETERS FOR THAT CHANNEL

Step 2: TB range	Step 3: Min CDF	10.65H Step 4: Poly order			18.7H Step 4: Poly order			23.8H Step 4: Poly order		
		1 st	2 nd	3 rd	1 st	2 nd	3 rd	1 st	2 nd	3 rd
± 10 K	1%	0.19	0.18	0.17	0.33	0.33	0.38	0.78	1.05	1.30
	2%	0.21	0.21	0.20	0.33	0.32	0.38	0.76	1.07	1.47
	3%	0.21	0.22	0.23	0.34	0.32	0.43	0.69	1.03	1.55
± 20 K	1%	0.17	0.19	0.19	0.31	0.35	0.36	0.60	0.69	0.85
	2%	0.17	0.20	0.22	0.34	0.41	0.52	0.52	0.61	0.82
	3%	0.16	0.20	0.24	0.33	0.39	0.53	0.53	0.69	1.15
± 30 K	1%	0.17	0.19	0.19	0.31	0.36	0.41	0.51	0.59	0.65
	2%	0.17	0.20	0.22	0.32	0.37	0.43	0.56	0.65	0.92
	3%	0.17	0.21	0.24	0.34	0.43	0.50	0.66	0.78	1.20

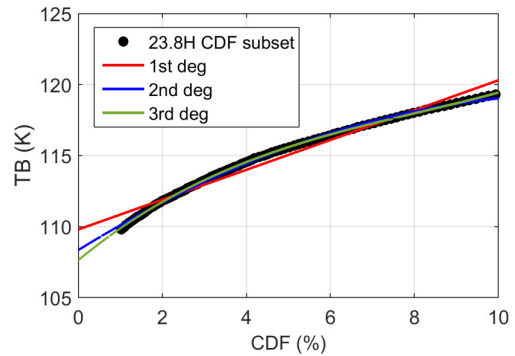


Fig. 4. 23.8 H CDF subset with first-, second-, and third-order polynomial fits. The linear fit is chosen as the best for the most stable cold cal TB since it is the least sensitive to small variations in the TBs near the cold end.

One observation from Table II is that the third-order polynomial does not give the most stable cold cal TB. This is the polynomial order used in the original algorithm but for these channels, especially 23.8 H, a first-order polynomial gives the most stable cold cal TB. Fig. 4 shows the CDF subset for 23.8 H with first- to third-order polynomial fits. For the channels that are less sensitive to geophysical variability such as 6.9 and 10.65 GHz, the choice of a first-, second-, or third-order polynomial gives very similar results for the cold cal TB stability. However, the channels that are more sensitive to small geophysical variations such as 23.8 H benefit from a polynomial fit of lower order that does not try to match the data so closely. While a third-order fit produces the smallest root mean squared error, a linear fit to the CDF results in the most stable cold cal TB and is therefore used for all channels in the VCC algorithm.

Another observation from Table II is that the TB range chosen for Step 2 cannot be the same at all the channels. The TB range chosen for Group 1 is ± 10 K (same as the original algorithm), for Group 2 it is ± 20 K, and for Group 3 it is ± 30 K. These ranges are chosen using the results from Table II as well as observations from Fig. 2. Choosing TB

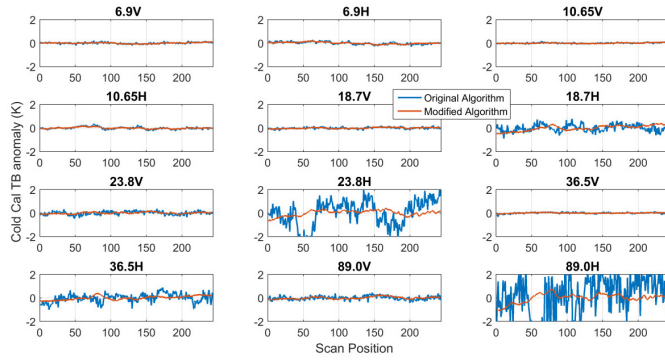


Fig. 5. Comparison of the cold cal TB across the scan for the original VCC algorithm (blue line) and the modified VCC algorithm (orange line). The modified VCC algorithm significantly improves the stability of the cold cal TB for some channels.

ranges of ± 10 , ± 20 , and ± 30 K for 10.65, 18.7, and 23.8 H, respectively, results in a histogram subset that roughly includes only TBs colder than the first relative maximum of the total histogram. These TBs are associated with low amounts of water vapor and SWS (see Section III).

Finally, Table II shows that using 1% as a minimum for the CDF range gives a slight improvement over 3%, so the CDF subset range is chosen to be 1%–10% for all the channels, a small modification from the original algorithm. It is possible to adjust this CDF range and achieve a slightly more stable cold cal TB by having different ranges for each channel. However, the small increase in stability that results is not considered significant enough to warrant using different VCC algorithms for each channel. In general, there is a desire to use a single VCC algorithm for all the channels and for different instruments. This standardization allows the VCC method to serve as a stable transfer standard between instruments.

Previous studies [3]–[5], [11] that applied VCC to conical scanners did not use all the four steps outlined here. These studies used a modified VCC algorithm that eliminated Step 2, instead finding a CDF subset of the total histogram (e.g., 1%–10%) and fitting a second-order polynomial to that subset. Step 2 is included in this version since it is found that using a histogram subset based on a TB range rather than a CDF range results in a slightly more stable cold cal TB for channels most sensitive to geophysical variability, such as 23.8 and 89 H. The analysis here also leads to the conclusion that using a first-order polynomial rather than a second-order gives the most stable cold cal TB.

D. VCC Algorithm Comparison

The modified VCC algorithm is applied along with the original algorithm to one month (July 2014) of AMSR2 simulations using a constant EIA across the scan. The cold cal TB as a function of scan position is shown in Fig. 5 for both the VCC algorithms. The scale is kept the same for all the channels to simplify comparison of the relative stability of the cold cal TB among the channels. Table III gives the mean and standard deviation of the cold cal TB across the 243 scan positions for both the algorithms. All the channels show a

TABLE III

MEAN AND STANDARD DEVIATION OF THE COLD CAL TB ACROSS THE SCAN, COMPARING THE ORIGINAL AND MODIFIED VCC ALGORITHM. THE MODIFICATIONS RESULT IN A LOWER STANDARD DEVIATION FOR ALL CHANNELS

Channel	Mean (K)			Standard Deviation (K)		
	Original Algorithm	Modified Algorithm	Difference	Original Algorithm	Modified Algorithm	Percent Improvement (%)
6.9V	149.9	150.1	0.2	0.08	0.05	40
6.9H	75.3	75.6	0.3	0.12	0.08	32
10.65V	156.9	157.1	0.2	0.05	0.03	35
10.65H	80.1	80.3	0.2	0.11	0.06	43
18.7V	173.0	173.2	0.2	0.09	0.05	46
18.7H	93.3	95.9	2.6	0.31	0.23	25
23.8V	183.9	185.2	1.3	0.16	0.07	58
23.8H	105.6	110.5	4.9	1.12	0.24	79
36.5V	200.9	201.2	0.3	0.07	0.03	54
36.5H	123.2	126.4	3.2	0.37	0.17	54
89.0V	233.3	234.8	1.5	0.20	0.10	45
89.0H	158.9	167.6	8.7	2.27	0.38	83

decrease in the standard deviation using the modified VCC algorithm. The mean is typically higher with the modified algorithm, which is attributed to using a linear fit rather than a third-order polynomial fit.

Ideally we would like the standard deviation to be less than 0.1 K, but this may not be possible with some of the channels most sensitive to small geophysical changes such as 23.8 and 89.0 H. This example is done using global TBs for July when the atmosphere in the Northern Hemisphere (NH) has high amounts of water vapor, leading to a less stable cold cal TB for the water vapor sensitive channels. The following section will explore whether it is possible to achieve a lower standard deviation using more TB samples.

E. Stability

The analysis in the previous section used a month of TB simulations to show the cold cal TB stability, but it was not stated whether a month is sufficient to achieve the best stability possible. This section will examine the dependence of the cold cal TB stability on TB sample number.

The cold cal TB is calculated for the AMSR2 simulations at each scan position starting with only one day of simulations and increasing the number of days used in the calculation up to 60. Simulations are used here as in the previous section so that the standard deviation of the cold cal TB across the scan can be used as a metric to analyze the stability of the cold cal TB. Fig. 6 shows the standard deviation using TB simulations for the specified number of days, starting with March 1 for the left plot and July 1 for the right plot. These cases are compared since they represent seasons with different geophysical parameter distributions, leading to contrasting behavior in the cold cal TB stability (see Section III for discussion of the geophysical parameter impact on VCC). July shows more instability in the cold cal TB since the

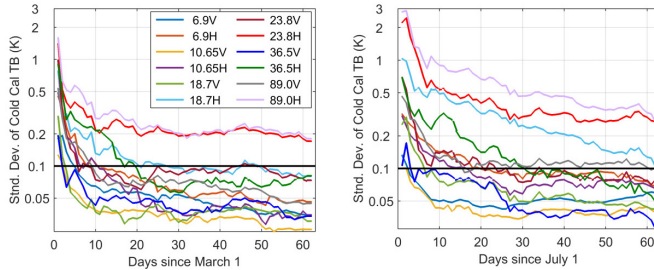


Fig. 6. Standard deviation of the simulated cold cal TB across the scan using an increasing number of daily observations. Data are plotted using a log scale for the standard deviation. The left plot is the number of days used starting with March 1 and the right plot is the number of days used starting with July 1. The black line indicates the 0.1 K threshold.

geophysical parameters that produce the coldest TBs have a greater variability than in March. While the VCC algorithm is designed to reduce the geophysical variable impact, it does not completely eliminate it (see Section IV for how to further reduce this impact).

As expected, the standard deviation decreases as the number of daily TB samples increases, and this behavior varies depending on the channel and season. The black line in each plot indicates the 0.1 K threshold. Most channels achieve stability better than 0.1 K using a month of data or less. The channels that have a harder time achieving 0.1 K stability within a month are 23.8 and 89.0 H for both the cases and 18.7 H for the July 1 start date. This analysis shows that for these channels, which are most sensitive to geophysical variability, it is necessary to use at least a month of TB samples to achieve stability in the cold cal TB. These results also indicate the timescale on which changes in instrument stability could be detected at the 0.1 K level.

III. ANALYSIS OF COLDEST TBs

The previous section described a modified VCC algorithm that achieves stability by minimizing dependence on geophysical parameters. VCC only uses the coldest TBs that are expected to be produced from global regions with low atmospheric water vapor and calm ocean surface winds. According to surface emission theory, at any given frequency, polarization, and EIA, there is a particular SST at which the surface upwelling TB is minimized. This would imply that the regions on earth that generate the coldest TBs and contribute to the calculation of the cold cal TB are determined by SST distribution. However, this assumes that SST variation is the only factor influencing the TBs and other geophysical variables such as atmospheric water vapor remain constant. This is obviously not a realistic assumption on earth. Atmospheric water vapor varies considerably on the globe, with higher amounts of water vapor typically correlated with higher SSTs. For channels most sensitive to water vapor, the water vapor variability should play a larger role in determining the global regions that produce the coldest TBs rather than SST alone.

This section discusses factors that influence the cold cal TB. Two factors are discussed: the global regions that produce the coldest TBs and the geophysical parameters that contribute to these cold TBs.

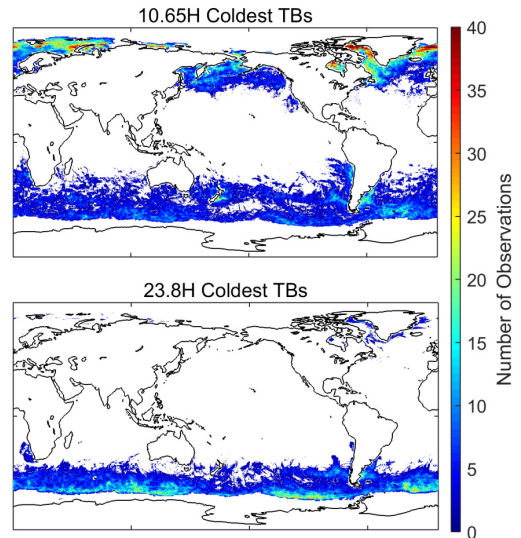


Fig. 7. Occurrence of AMSR2 10.65 H (top) and 23.8 H (bottom) coldest TBs from the CDF subset for July 2014 over-ocean data. Colors indicate the number of observations that fall into a 0.1° grid.

A. Regions of Coldest TBs

The VCC algorithm bins all over-ocean TBs into a histogram and uses the coldest part of the histogram to calculate the cold cal TB. Since no regional filter is used on the data, it is impossible to know which regions on earth are contributing to the coldest part of the histogram without further analysis. One benefit to knowing which regions contribute to the coldest TBs is to aid in identifying instabilities that may occur in the cold cal TB due to regional differences. For example, the coldest regions can change with season, thereby affecting the value of the cold cal TB. If this is not properly accounted for, it could be taken as a calibration error. Also, if a radiometer does not observe certain regions due to characteristics of the orbit or missing data, it is important to know how these missing regions from the data set may impact the cold cal TB.

The coldest TB observations from AMSR2 for July 2014 are gridded into 0.1° boxes to analyze the regions producing the coldest TBs. The coldest observations are those that make up the CDF subset used to derive the cold cal TB as described in Section II. Fig. 7 shows the regions with the coldest TBs for two channels: 10.65 and 23.8 H. These channels are chosen since they show very different characteristics for the coldest regions. Colors indicate the number of observations that fall into a 0.1° grid.

Fig. 7 shows that the coldest TBs are produced from regions closest to the poles. The southern and northern extents of the coldest TBs are determined by sea ice, as can be seen most strongly in the Southern Hemisphere (SH). In the NH the cold TBs can be found quite far north since the sea ice in the NH does not extend very far south in July. 23.8 H shows a strong preference for the SH with 99% of the coldest TBs from the SH, while 10.65 H is more evenly distributed between the hemispheres with 49% of the coldest TBs from the SH. During NH summer, there is a high water vapor content in the NH which pushes the coldest TBs to the SH where there is less

water vapor. 10.65 H is not as sensitive to water vapor, so the distribution of the coldest TBs is more even between the two hemispheres.

The regions that produce the coldest TBs can change throughout the year due to the seasonal variability of the geophysical parameters (e.g., atmospheric water vapor). Performing the same analysis for January 2014 yields very different results. The percentage of the coldest TBs that occur in the SH is 71% and 27% for 10.65 and 23.8 H, respectively. This shows that the regions where the cold cal TB is derived can change seasonally, which may impact the value of the cold cal TB (see Section IV).

B. Geophysical Parameters of Coldest TBs

The previous section showed which regions produce the coldest TBs and that the regions can vary considerably depending on the frequency, polarization, and season. This section takes the analysis a step further and looks at the geophysical parameters that contribute to the coldest TBs. GDAS is used to find the SST, IWV, and SWS values that are associated with each TB observation, using the closest grid point in space and time. These values are binned into histograms for all observations. Histograms of the geophysical variables associated with the coldest TBs in the CDF subset for each channel are also generated so that a comparison can be made between the geophysical variables contributing to the coldest TBs versus all TB observations.

The results of this paper are shown in Fig. 8 for the 10.65 and 23.8 H channels. These two channels are shown since it is expected that 10.65 H is more sensitive to the surface while 23.8 H is more sensitive to atmospheric water vapor. Fig. 8 gives some important insights into the geophysical variables that impact VCC. First, Fig. 8(a) confirms that SST plays a very minor role in determining the cold cal TB. The coldest TB histograms show no bias toward the SST that produces theoretically the lowest TBs for the channels (SST of 273 K for 10.65 H and 288 K for 23.8 H). Second, Fig. 8(b) confirms that the cold cal TB is derived from regions with minimal water vapor. The two channels do show a slight difference in the coldest histograms. It appears that the 10.65 H channel allows the water vapor to be slightly higher than for 23.8 H. This can most likely be explained by Fig. 8(c), which shows the wind speed histograms. 10.65 H has a cold TB histogram with a mean wind speed that is slightly lower than 23.8 H, most likely indicating that the 10.65 H coldest TBs are allowed to have a little more water vapor in favor of having a lower wind speed.

Table IV gives the mean SST, IWV, and SWS for the CDF subset coldest TBs for each AMSR2 channel. The mean is a good representation of the actual values that impact the cold cal TB since all the TBs from the CDF subset are used in the derivation of the cold cal TB (see Fig. 4). The mean SST for all the channels is within a 10 K range, suggesting that SST does not play a large role in determining the cold cal TB since the mean SST does not vary greatly with frequency. On the other hand, the IWV is less than or equal to 1.0 cm for all frequencies above 10.65 GHz, which indicates that the

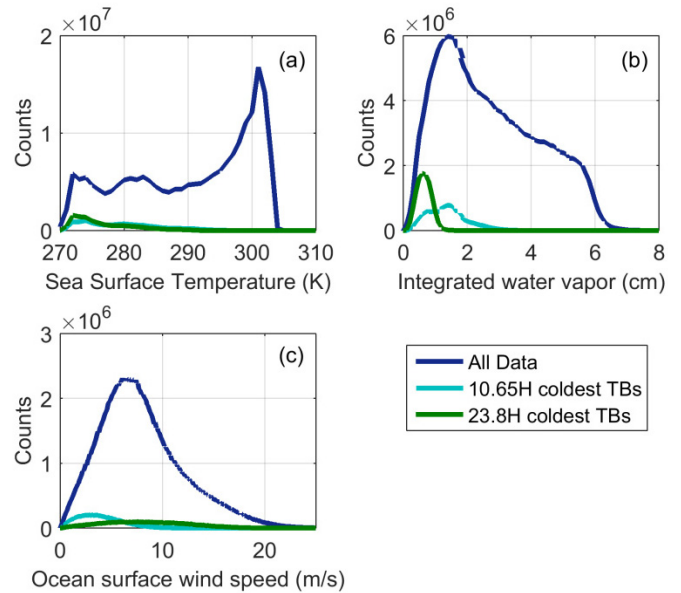


Fig. 8. Histograms of the GDAS SST (a) IWV, (b) SWS, and (c) for July 2014 AMSR2 observations using all over-ocean data compared with the coldest TBs for 10.65 and 23.8 H.

TABLE IV
MEAN SST, IWV, AND SWS VALUES ASSOCIATED WITH THE TBs USED TO DERIVE THE COLD CAL TB FOR AMSR2 JULY 2014 OBSERVATIONS

Channel	SST (K)	IWV (cm)	SWS (m/s)
6.9V	273.8	1.0	7.2
6.9H	277.9	1.4	4.5
10.65V	274.9	1.0	6.6
10.65H	279.1	1.4	3.8
18.7V	276.4	0.7	7.5
18.7H	278.4	0.8	5.6
23.8V	275.5	0.6	9.3
23.8H	275.9	0.6	7.8
36.5V	278.7	0.8	9.0
36.5H	281.0	1.0	5.0
89.0V	274.8	0.6	12.3
89.0H	275.7	0.6	8.1

coldest TBs are from regions with minimal atmospheric water vapor. Table IV also shows that at all frequencies, the H-pol channel has a lower mean SWS than the V-pol channel but a slightly higher IWV. According to the Meissner and Wentz model [7], the surface TB initially decreases with increasing SWS for all AMSR2 V-pol channels while the H-pol surface TB increases with increasing SWS. The H-pol channels also show a greater sensitivity to SWS than the V-pol channels, especially at low SWS. This explains the behavior in Table IV in which the H-pol channels allow the IWV to be somewhat higher than the V-pol channels in favor of a lower SWS. This analysis also shows that SST variation does not play a large role in the cold cal TB, while the IWV appears to be the most important geophysical parameter for determining the cold cal TB.

IV. APPLICATION TO MICROWAVE IMAGER OBSERVATIONS

This section demonstrates the VCC algorithm's performance when applied to microwave imager observations. One important aspect of using VCC as a calibration tool is that simulated TBs are required alongside the observed TBs to calculate the single difference (SD), the observed cold cal TB minus the simulated cold cal TB. The SD is used to account for instrument characteristics such as EIA variation and to reduce seasonal and diurnal variations that may exist in the observed cold cal TB, providing a more stable calibration reference [4]. This section also discusses some further filtering of the observed TBs that is required when applying the VCC algorithm to low-inclination orbiters since these imagers do not observe all the latitudes.

A. Simulations

It has been previously shown that simulated TBs are necessary when using VCC as a calibration tool for a microwave radiometer [4]. The simulations are able to account for geophysical (e.g., seasonal) variability and instrumental (e.g., nonconstant EIA) characteristics that impact the observed TBs. Through the SD, these characteristics are accounted for so that the VCC algorithm can be used as a relative calibration reference.

Simulated TBs are generated for each radiometer pixel over the ocean. GDAS is used to obtain the input atmospheric profiles and surface conditions, along with land and sea ice flags so that only open-ocean pixels are simulated. A clear-sky filter from GDAS is used to help reduce the number of radiometer pixels that need to be simulated without impacting the cold cal TB stability. The clear-sky filter removes all data where the GDAS liquid water path is greater than 0 kg/m², typically about 50% of the global over-ocean data. The GDAS clear-sky filter does not accurately identify all clouds, so further filtering based on the TBs is necessary for the frequencies near 90 GHz to remove the very cold observed TBs due to hydrometeor scattering [11].

B. Regional Single Difference

One concern identified in Section III is that the regions that produce the coldest TBs change seasonally, with some channels impacted more than others. The example given in Section III found that 99% of the coldest 23.8 H TBs are located in the SH for the month of July and this percentage drops to 27% for January. If just the observed cold cal TB is used as a calibration reference, this regional change due to seasonal variations may cause instability in the cold cal TB that could get taken as an instrument calibration error [4]. Incorporating modeled TBs through the SD accounts for the seasonal variability, so it is not included in the calibration reference.

To test the impact of regional and seasonal variability on VCC, the SD is calculated for the NH and SH separately and also for the globe for one year of AMSR2 data. It is determined that there is no significant difference between taking the average of the NH and SH SDs versus calculating the SD for global data. This shows that the VCC algorithm

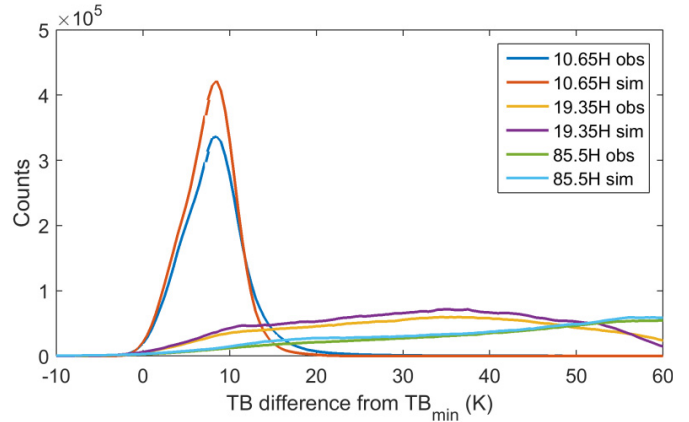


Fig. 9. TMI observed and simulated TB histograms for 10.65, 19.35, and 85.5 H for July 2014 where TB_{min} for each channel is 82.2, 107.2, and 188.1 K, respectively. The observed and simulated total TB histograms are different but the cold end shapes are similar.

is indeed robust and able to absorb differences in the regional TB values using the SD.

C. Low-Inclination Orbiters

The previous analyses have focused on AMSR2, which is on-board a sun-synchronous orbiter able to provide observations at all latitudes. Low-inclination orbiters, such as the Tropical Rainfall Measuring Mission (TRMM) carrying the TRMM Microwave Imager (TMI), do not observe all latitudes. This can impact how the VCC algorithm is implemented.

There are two major concerns with microwave imagers on low-inclination orbiters. First, the imagers do not observe all latitudes and therefore may not see the regions of the coldest TBs shown in Fig. 7, depending on how shallow the orbit is. This impacts both the shape of the TB histogram and the stability of the cold cal TB, since observations of regions with high water vapor comprise a greater proportion of the TB histogram than for sun-synchronous orbiters. A comparison of TMI observed and simulated TB histograms is given in Fig. 9 to show that the shape at the cold end is similar. The cold end shapes are also comparable to AMSR2 (see Fig. 3), so the modified VCC algorithm developed using AMSR2 histograms will perform similarly when applied to TMI or other low-inclination orbiters. The stability of the cold cal TB is also a concern with the shallow orbit. Kroodsma *et al.* [4] showed that there is a slight seasonal cycle evident in the SD for the TMI water vapor channel that is not present in the water vapor channel for a sun-synchronous orbiter observing all latitudes. This may indicate that the simulations are not able to accurately model the water vapor burden in the tropics. The simulations therefore need to be evaluated as a potential source of uncertainty when using the VCC SD as a calibration reference.

The second concern with low-inclination orbiters is the scan position sampling. The TMI scan geometry coupled with the lower inclination results in uneven scan sampling at the higher latitudes, as can be seen in Fig. 10(a). Fig. 10(a) shows the TMI scan position and latitude sampling for TMI in the

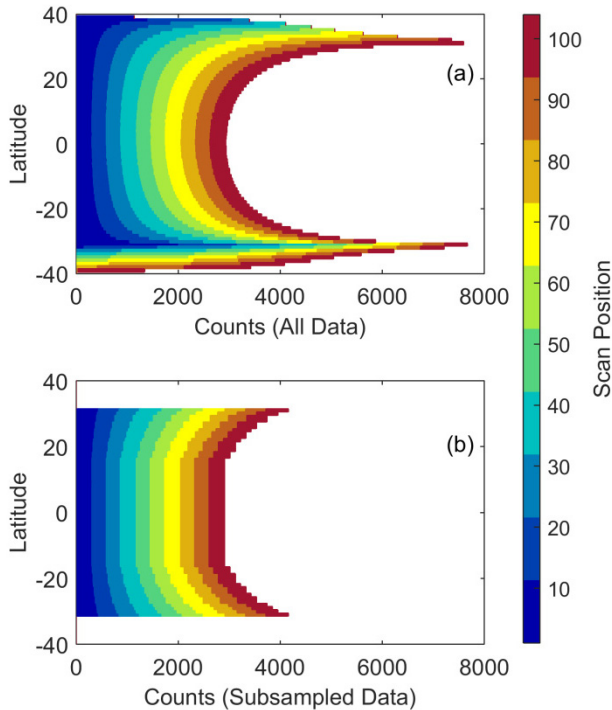


Fig. 10. Latitude and scan position sampling for TMI yaw 0 orientation using all data (top) and subsampled data (bottom) so that there is uniform sampling at all scan positions in 1° latitude intervals. The asymmetry noted when all data are used is caused by differences in sampling of the highest northern and southern latitudes due to the off-nadir pointing geometry of the instrument.

yaw 0 orientation. As a nonsun-synchronous orbiter, TRMM undergoes a 180° yaw maneuver approximately every 21 days to keep the solar panels oriented properly with respect to the sun. In the yaw 0 orientation the high scan positions see farther south while the low scan positions see farther north. The pattern reverses when the spacecraft is in the yaw 180 orientation. This scan sampling pattern causes a bias in the observed cold cal TB since one edge of the scan is able to see farther north/south and can observe colder TBs than the other edge of the scan. If this bias is not properly identified as a geophysical effect, it could be mistaken for an error in the across-scan calibration.

To eliminate the uneven scan sampling impact, the TBs for each scan position are filtered into 1° latitude bins and forced to have an even sampling across the scan, as shown in Fig. 10(b). TBs are randomly filtered to create the even scan sampling at each latitude bin. One drawback to this, as seen in Fig. 10(b), is that the latitude range of observations used for calculating the cold cal TB is greatly reduced from approximately $\pm 40^\circ$ to $\pm 31^\circ$. As discussed, this can cause greater instability in the cold cal TB since it forces the VCC algorithm to use the TBs closer to the tropics that contain higher amounts of water vapor. However, if this process is not done, the result is a scan bias in the cold cal TB that is geophysical in nature rather than an instrument calibration error.

Fig. 11 shows the TMI 10.65 V yaw 0 SH observed cold cal TB (top) and the SD (bottom) for the two cases of:

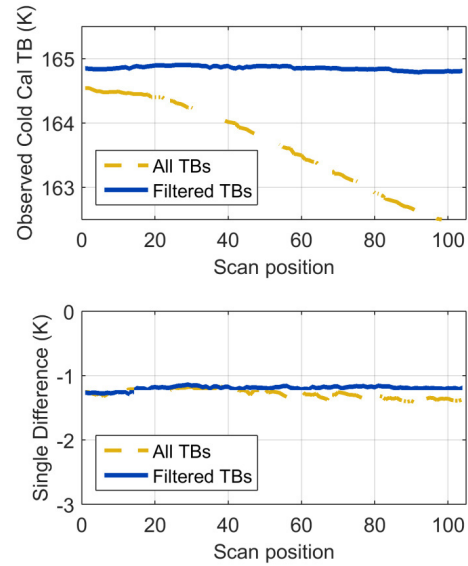


Fig. 11. Observed cold cal TB (top) and SD (bottom) for TMI 10.65 V at yaw 0 comparing the VCC algorithm results when using all over-ocean TBs (yellow dashed line) versus filtering the TBs to have similar sampling by scan position and latitude (blue solid line).

1) using all data and 2) using subsampled data with uniform scan position sampling. There is a downward trend in the observed cold cal TB when using all of the TBs (yellow dashed line) since the higher scan positions see farther south than the lower scan positions. This results in about a 2 K difference from one side of the scan to the other. If this is not properly identified as a feature of the instrument scanning geometry, this could be taken as a calibration error. By subsampling the TB observations using the previously described method, the result is the blue solid line in Fig. 11. The SD shows that the simulations that have the same subsampling as the observations are able to almost exactly model the scan bias in the observed cold cal TB. However, there is still a slight discrepancy in the SD on the right side of the scan, which means the simulations do not exactly model reality. Filtering the TBs to have a uniform scan position sampling at each latitude is an important step to perform when using the VCC algorithm on low-inclination orbiters.

V. VALIDATION USING INTERCALIBRATION DOUBLE DIFFERENCE METHOD

VCC is valuable as an intercalibration algorithm since it is independent of other intercalibration methods and can therefore be used to corroborate the intercalibration results. The major difference between VCC and other intercalibration techniques is that VCC does not require filtering of the radiometer TBs to only include pixels where the ground tracks of the instruments cross each other (referred to as the match-up method). VCC is one of the algorithms used in the Global Precipitation Measurement's (GPM) microwave radiometer intercalibration algorithm [12], [13]. VCC is an integral part of the GPM intercalibration algorithm since it provides an independent result from the other intercalibration techniques that use the match-up method.

TABLE V

INTERCALIBRATION RESULTS FOR TMI COMPARED WITH WINDSAT FOR JULY 2005–JUNE 2006. THE VCC ALGORITHM SHOWS GOOD AGREEMENT WITH THE OTHER TWO METHODS

Channel	Biswas <i>et al.</i> [14]		Wilheit [15]		VCC	
	DD (K)	Temp (K)	DD (K)	Temp (K)	DD (K)	Temp (K)
10V	0.26	170	0.33	171	0.30	166
10H	-1.62	88	-1.69	89	-1.67	83
19V	-0.56	199	-0.88	202	-0.94	184
19H	-2.84	132	-3.02	137	-3.03	110
21V	-1.77	219	-1.52	224	-1.71	197
37V	-3.23	214	-3.19	216	-3.27	204
37H	-2.51	152	-2.47	156	-2.51	135

The method of using the VCC algorithm for microwave radiometer intercalibration is described in [4]. This section will show that the VCC algorithm as an intercalibration method compares well with other intercalibration techniques.

A. VCC Comparison With Other Methods

Table V shows the results from Biswas *et al.* [14], Wilheit [15], and the VCC algorithm for TMI-WindSat double differences for July 2005–June 2006. The double difference (DD) and the TB at which the DD is calculated (Temp) are both shown. Biswas *et al.* [14] use the match-up method of intercalibration with GDAS as inputs to the RTM. Wilheit [15] also uses the match-up method, but he computes the geophysical parameters for the RTM using a least squares fit method. Most of the channels show agreement among the three methods to within 0.2 K. One characteristic of the VCC algorithm that can be seen in Table V is that VCC typically derives a DD value at a colder TB than the match-up method. This is due to VCC only using the coldest TBs with minimal water vapor, while the DD calculated from the match-up method typically includes TBs with higher levels of water vapor, which results in higher TB values. Table V verifies that even though the VCC algorithm uses a very different algorithm to calculate double differences, it achieves similar results.

Since WindSat does not include a high-frequency (near 90 GHz) channel, the previous analysis could not compare the performance of VCC at that frequency. Alswiss *et al.* [16] calculated DDs for TMI compared with AMSR2 for January 2013–April 2013. Their results along with the VCC algorithm's results are shown in Table VI. Alswiss *et al.* [16] calculated DDs for AMSR2 separated into ascending and descending orbit nodes and the average of these two nodes is reported here. Significant differences between the two methods are seen for the 19 V, 19 H, and 21 V channels. One explanation for this difference is the DD dependence on temperature. Alswiss *et al.* [16] do not report a temperature for their DDs, however, they do include a figure

TABLE VI

TMI-AMSR2 DOUBLE DIFFERENCES FOR JANUARY 2013–APRIL 2013 [16] DO NOT INCLUDE A TEMPERATURE WITH THEIR RESULTS SO THAT IS NOT INCLUDED HERE

Channel	Alswiss <i>et al.</i> [16]	VCC	
	DD (K)	DD (K)	Temp (K)
10V	4.0	4.1	166
10H	4.7	5.0	83
19V	3.3	4.3	183
19H	1.9	3.7	109
21V	3.4	4.2	196
37V	3.6	4.0	204
37H	4.4	4.8	134
85V	1.1	1.4	245
85H	2.4	2.8	192

illustrating the DD dependence on TB. Their analysis shows a strong DD dependence on TB for the 19 V, 19 H, and 21 V channels, and the VCC results at the reported temperatures line up very closely with what they report. Discrepancies between the two methods may also be explained by the lack of sufficient data, since only four months are used to calculate the DD. The previous comparison with TMI-WindSat used a year of data.

The consistency of the results using the VCC DD with the other intercalibration methods shows that it is a valid and accurate method to use for the intercalibration of spaceborne microwave imagers.

B. Stability of VCC Double Difference

The previous section showed the results of the VCC DD method that were calculated by first finding the DD for each month, and then taking the average of the monthly DDs. This was done for ease of calculation since filtering the data into monthly histograms is convenient. However, as shown in Section II, a month of data may not achieve the most stable cold cal TB for some channels. An analysis is done to see if averaging the monthly results gives the most stable DD, or if a different time period is more appropriate.

The mean and standard deviation of the VCC DD is calculated for one year of data, comparing weekly, monthly (shown in the previous section), and bimonthly filtering of the data. As expected, the standard deviation of the DD decreases as more data are used to calculate the DD. The mean, on the other hand, shows no significant change. The mean DD is the quantity that is used for intercalibration purposes and this analysis shows that the time period used for calculation of the VCC DD does not impact the intercalibration.

VI. CONCLUSION

VCC for application to conical scanning microwave imagers was presented. Modifications were made to the original algorithm to achieve a robust calibration reference for conical

scanners with frequencies from 6 to 90 GHz. The VCC algorithm was divided into four steps and each was analyzed for modification. These steps involve the calculation of the first-guess (Step 1), the TB range chosen from the first-guess to create a histogram subset of cold TBs (Step 2), the CDF range of the histogram subset (Step 3), and finally the polynomial order used to derive the cold cal TB (Step 4). The standard deviation of simulated TBs across the radiometer scan was used as a metric for stability since the simulated cold cal TB should be constant across the scan. The parameters in Steps 1–4 were varied and the values that resulted in the lowest standard deviation across the scan were chosen for the modified VCC algorithm. The modified algorithm was shown to achieve a more stable calibration than the original one that was designed for a nadir-viewing radiometer. Some channels were able to achieve a greater stability than other channels due to the characteristics of individual channels. The channels categorized in Group 1 (6.925 V/H, 10.65 V/H, 18.7 V, and 36.5 V) are the least sensitive to small geophysical variations, resulting in a more stable cold cal TB than those channels in Group 2 (18.7 H, 23.8 V, 36.5 H, and 89.0 V) and Group 3 (23.8 and 89.0 H). The Group 2 and Group 3 channels require a data set with a longer time period to reduce noise in the cold cal TB but are still unable to achieve the level of stability obtained with the Group 1 channels.

The modified VCC algorithm was analyzed for dependence on the geophysical and regional variability. It was found that the coldest TBs contributing to the calculation of the cold cal TB are determined largely by atmospheric water vapor distribution. Since the coldest TBs are determined by the water vapor variability, the regions where the coldest TBs are produced can vary greatly with season. Any seasonal dependence in VCC is accounted for by taking the difference between the cold cal TB calculated from observations and the cold cal TB calculated from modeled TBs. This results in the SD that can be used as a relative calibration reference for a radiometer. The VCC SD was applied to TMI, a nonsun-synchronous orbiter in a shallow orbit inclination. It was determined necessary to subsample the data to have consistent sampling by latitude across the scan to remove any sampling error in the VCC SD.

Finally, VCC was shown to be an accurate microwave intercalibration method by calculating the VCC DD and comparing with other intercalibration methods. The VCC DD was calculated for both WindSat and AMSR2 compared with TMI and in both the cases was shown to agree well with previously published results that use the match-up method for intercalibration. This demonstrated that the modified VCC algorithm is a valid method to be used as a calibration reference for conically scanning microwave imagers.

REFERENCES

- [1] C. S. Ruf, "Detection of calibration drifts in spaceborne microwave radiometers using a vicarious cold reference," *IEEE Trans. Geosci. Remote Sens.*, vol. 38, no. 1, pp. 44–52, Jan. 2000.
- [2] C. S. Ruf, "Characterization and correction of a drift in calibration of the TOPEX microwave radiometer," *IEEE Trans. Geosci. Remote Sens.*, vol. 40, no. 2, pp. 509–511, Feb. 2002.
- [3] D. S. McKague, C. S. Ruf, and J. J. Puckett, "Beam spoiling correction for spaceborne microwave radiometers using the two-point vicarious calibration method," *IEEE Trans. Geosci. Remote Sens.*, vol. 49, no. 1, pp. 21–27, Jan. 2011.
- [4] R. A. Kroodasma, D. S. McKague, and C. S. Ruf, "Inter-calibration of microwave radiometers using the vicarious cold calibration double difference method," *IEEE J. Sel. Topics Appl. Earth Observ. Remote Sens.*, vol. 5, no. 3, pp. 1006–1013, Jun. 2012.
- [5] M. R. P. Sapiano, W. K. Berg, D. S. McKague, and C. D. Kummerow, "Toward an intercalibrated fundamental climate data record of the SSM/I sensors," *IEEE Trans. Geosci. Remote Sens.*, vol. 51, no. 3, pp. 1492–1503, Mar. 2013.
- [6] K. Imaoka *et al.*, "Global change observation mission (GCOM) for monitoring carbon, water cycles, and climate change," *Proc. IEEE*, vol. 98, no. 5, pp. 717–734, May 2010.
- [7] T. Meissner and F. J. Wentz, "The emissivity of the ocean surface between 6 and 90 GHz over a large range of wind speeds and earth incidence angles," *IEEE Trans. Geosci. Remote Sens.*, vol. 50, no. 8, pp. 3004–3026, Aug. 2012.
- [8] P. W. Rosenkranz, "Water vapor microwave continuum absorption: A comparison of measurements and models," *Radio Sci.*, vol. 33, no. 4, pp. 919–928, Jul./Aug. 1998.
- [9] H. J. Liebe, P. W. Rosenkranz, and G. A. Hufford, "Atmospheric 60-GHz oxygen spectrum: New laboratory measurements and line parameters," *J. Quant. Spectrosc. Radiat. Transf.*, vol. 48, nos. 5–6, pp. 629–643, 1992.
- [10] CISM Data Support Section at the National Center for Atmospheric Research, Boulder, CO, USA. (Aug. 2014). *U.S. National Centers for Environmental Prediction, Updated Daily: NCEP FNL Operational Model Global Tropospheric Analyses, Continuing From July 1999. Dataset ds083.2*. [Online]. Available: <http://dss.ucar.edu/datasets/ds083.2/>
- [11] R. A. Kroodasma, D. S. McKague, and C. S. Ruf, "Extension of vicarious cold calibration to 85–92 GHz for spaceborne microwave radiometers," *IEEE Trans. Geosci. Remote Sens.*, vol. 51, no. 9, pp. 4743–4751, Sep. 2013.
- [12] T. Wilheit *et al.*, "Intercalibrating the GPM constellation using the GPM microwave imager (GMI)," in *Proc. IEEE Int. Geosci. Remote Sens. Symp. (IGARSS)*, Milan, Italy, Jul. 2015, pp. 5162–5165.
- [13] A. Y. Hou *et al.*, "The global precipitation measurement mission," *Bull. Amer. Meteorol. Soc.*, vol. 95, no. 5, pp. 701–722, May 2014.
- [14] S. K. Biswas, S. Farrar, K. Gopalan, A. Santos-Garcia, W. L. Jones, and S. Bilanow, "Intercalibration of microwave radiometer brightness temperatures for the global precipitation measurement mission," *IEEE Trans. Geosci. Remote Sens.*, vol. 51, no. 3, pp. 1465–1477, Mar. 2013.
- [15] T. T. Wilheit, "Comparing calibrations of similar conically scanning window-channel microwave radiometers," *IEEE Trans. Geosci. Remote Sens.*, vol. 51, no. 3, pp. 1453–1464, Mar. 2013.
- [16] S. O. Alsweiss, Z. Jelenak, P. S. Chang, J. D. Park, and P. Meyers, "Inter-calibration results of the Advanced Microwave Scanning Radiometer-2 over ocean," *IEEE J. Sel. Topics Appl. Earth Observ. Remote Sens.*, vol. 8, no. 9, pp. 4230–4238, Sep. 2015.



Rachael A. Kroodasma (S'09–M'14) received the B.S.E. degree in earth systems science and engineering, the M.S.E. degree in electrical engineering, and the Ph.D. degree in atmospheric, oceanic, and space sciences from the University of Michigan, Ann Arbor, MI, USA, in 2009, 2013, and 2014, respectively.

She is currently a Post-Doctoral Associate with the Earth System Science Interdisciplinary Center, University of Maryland, College Park, MD, USA. She is with the Precipitation Processing System at NASA Goddard Space Flight Center, Greenbelt, MD, USA. As a member of the Global Precipitation Measurement (GPM) inter-calibration working group (XCAL), she works on developing inter-calibration techniques and monitoring the calibration of the GPM constellation microwave radiometers. Her current research interests include microwave radiometer calibration and remote sensing of the atmosphere.



Darren S. McKague received the Ph.D. degree in astrophysical, planetary, and atmospheric sciences from the University of Colorado, Boulder, CO, USA, in 2001.

He was a Systems Engineer at Ball Aerospace, Boulder, CO, USA, and Raytheon, Aurora, CO, USA, and a Research Scientist at Colorado State University, Fort Collins, CO, USA. He was involved in remote sensing with an emphasis on the development of space-borne microwave remote sensing hardware, passive microwave calibration techniques,

and on mathematical inversion techniques for geophysical retrievals. He is an Associate Research Scientist with the Department of Climate and Space Sciences and Engineering, University of Michigan, Ann Arbor, MI, USA. His experience with remote sensing hardware includes systems engineering for several advanced passive and active instrument concepts and the design of the calibration subsystem on the Global Precipitation Mission (GPM) Microwave Imager as well as the development of calibration and inter-calibration techniques for the GPM constellation. His algorithm experience includes the development of a near-real time algorithm for the joint retrieval of water vapor profiles, temperature profiles, cloud liquid water path, and surface emissivity for the Advanced Microwave Sounding Unit at Colorado State University, and the development of the precipitation rate, precipitation type, sea ice, and sea surface wind direction algorithms for the risk reduction phase of the Conical scanning Microwave Imager/Sounder.



Christopher S. Ruf (S'85–M'87–SM'92–F'01) received the B.A. degree in physics from Reed College, Portland, OR, USA, and the Ph.D. degree in electrical and computer engineering from the University of Massachusetts at Amherst, Amherst, MA, USA.

He was with Intel Corporation, Aloha, OR, USA, Hughes Space and Communication, El Segundo, CA, USA, the NASA Jet Propulsion Laboratory, Pasadena, CA, USA, and Pennsylvania State University, State College, PA, USA. He is currently a

Professor of Atmospheric Science and Electrical Engineering at the University of Michigan, Ann Arbor, MI, USA, and a Principal Investigator of the Cyclone Global Navigation Satellite System NASA Earth Venture mission. His current research interests include GNSS-R remote sensing, microwave radiometry, atmosphere and ocean geophysical retrieval algorithm development, and sensor technology development.

Dr. Ruf is a member of the American Geophysical Union, the American Meteorological Society, and the Commission F of the Union Radio Scientifique Internationale. He was the Editor-in-Chief of the IEEE TRANSACTIONS ON GEOSCIENCE AND REMOTE SENSING, and has served on the editorial boards of *Radio Science* and the *Journal of Atmospheric and Oceanic Technology*. He has been a recipient of four NASA Certificates of Recognition and seven NASA Group Achievement Awards, as well as the 1997 TGRS Best Paper Award, the 1999 IEEE Resnik Technical Field Award, the 2006 IGARSS Best Paper Award, and the 2014 IEEE GRS-S Outstanding Service Award.